International Journal of Hydrogen Energy 152 (2025) 150172

Contents lists available at ScienceDirect

International Journal of Hydrogen Energy

journal homepage: www.elsevier.com/locate/he

# Tailoring rapid thermal synthesis of Pt-based alloy nanoparticles on carbon support for hydrogen evolution reaction

Huanqing Zhang [a,*], Stefan Manuel Noisternig [b], Qixiang Jiang [c], Martin Šala [d], Daniel Bautista – Anguis [e], Zequn Zhang [b], Stefan Wurster [b], Adam Elbataioui [a], Kaikai Song [f], Christian Rentenberger [g], Lidija D. Rafailović [b,**], Jürgen Eckert [a,b]

[a] Department of Materials Science, Montanuniversität Leoben, Leoben, Austria
[b] Erich Schmid Institute of Materials Science, Austrian Academy of Sciences, Leoben, Austria
[c] Institute for Materials Chemistry and Research, University of Vienna, Vienna, Austria
[d] Department of Analytical Chemistry, National Institute of Chemistry, Ljubljana, Slovenia
[e] Polymer Competence Center Leoben, Leoben, 8700, Austria
[f] School of Mechanical, Electrical & Information Engineering, Shandong University, Weihai, China
[g] Faculty of Physics, Physics of Nanostructured Materials, University of Vienna, Vienna, Austria

ARTICLE INFO

Handling Editor: Prof I Tolj

*Keywords:*
Carbothermal shock
Pt-based alloy NPs
Carbon felt substrate
PtNiRu catalyst
Hydrogen evolution

ABSTRACT

The controlled integration of multiple immiscible elements into Pt alloy nanoparticles (NPs) to develop novel electrocatalysts presents significant potential for advancing sustainable energy technologies. In this study, we use a simple method for mixing diverse metal elements from their precursor salt solutions to form alloy NPs. The synthesis was carried out by subjecting a mixture of precursor metal salts supported on carbon paper (CP) to thermal shock, rapidly increasing the temperature to ~ 1600 K. By modulating the types and numbers of metal elements, we synthesized multicomponent metal NPs with tailored chemical compositions and sizes. To validate the practical application of this catalyst, we evaluated its hydrogen evolution reaction (HER) activity during water splitting under acidic conditions. The synthesized CP-PtNiRu electrocatalyst demonstrates an overpotential of 30.5 mV at a current density of 10 mA/cm$^2$, comparable to that of commercial Pt/C electrodes, significantly enhancing the utilization efficiency of Pt-based electrocatalysts.

## 1. Introduction

According to ⟪OUR WORLD IN DATA⟫, as of 2023, fossil fuels (coal, oil, and natural gas) accounted for approximately 80 % of global energy consumption. However, the detrimental effects of fossil fuel combustion cannot be overlooked: greenhouse gas emissions, acidic rain, and other associated impacts pose severe threats to both the environment and human health. As a result, the global energy transition is gaining significant momentum. To further promote the development of renewable energy and reduce emissions, manifold efforts are underway to explore new alternative energy sources [1–5]. Notably, the earth's abundant water resources provide a sustainable foundation for hydrogen production. The process of water electrolysis holds immense potential for integration with renewable energy, offering a promising pathway for sustainable hydrogen generation [6–10].

In recent years, research on electrocatalyst material systems for the HER in water splitting has mainly focused on platinum-based catalysts [11–16]. Regrettably, the high cost and scarcity of Pt pose severe obstacles to its commercial utilization. Therefore, optimizing the utilization efficiency of Pt while maintaining catalytic efficacy and systematically designing catalysts based on a comprehensive understanding of their operational mechanisms constitute primary innovations of the current research endeavors [17–21]. To address this challenge, the incorporation of additional metallic elements into Pt to synthesize Pt-based metal NPs stands out as a highly effective approach for significantly enhancing the catalytic performance of Pt-based electrocatalysts. This method leverages the synergistic effects between platinum and the added metals, which can optimize electronic structures and modify surface properties, thereby promoting catalytic efficiency [22,23]. Among the diverse array of metals with varying properties,

* Corresponding author.
** Corresponding author.
*E-mail addresses:* huanqing.zhang@stud.unileoben.ac.at (H. Zhang), lidija.rafailovic@oeaw.ac.at (L.D. Rafailović).

https://doi.org/10.1016/j.ijhydene.2025.150172
Received 31 December 2024; Received in revised form 20 June 2025; Accepted 25 June 2025
Available online 4 July 2025

transition metals represent ideal mixed alloying candidates to substitute precious metals, owing to their economic viability and accessibility [24–26]. Gao et al. achieved mixed platinum with transition metals such as iron, cobalt, and nickel [14]. This method not only has the potential to enhance performance but also increases the dispersion of platinum and reduces its usage, thereby improving the overall cost-effectiveness of the catalyst. Simultaneously, they found that transition metals possess exceptional water adsorption and dissociation capabilities, which contributes to the establishment of a proton-rich local environment adjacent to platinum-based mixed metals, thereby facilitating HER performance. Yang et al. combined Pt single atoms ($Pt_{SA}$) with CoPt-mixed metal nanocrystals into MOF-derived nitrogen-doped porous-carbon framework (NDPCF), designing a new class of single-atom catalysts (SACs) [27]. The results demonstrated that the electrocatalyst has ultralow overpotentials at high current densities of −300 mA $cm^{-2}$ under both alkaline and acidic conditions and exhibits excellent long-term durability of up to 100 h or 10000 cycles, which is attributed to the synergistic effect of $Pt_{SA}$ and CoPt alloys in the NDPCF. Pan et al. presented a procedural research aimed at evaluating the electrocatalytic activity of High-entropy alloys (HEAs) prepared in one step by pulsed high-temperature synthesis technique, and indicating the contribution of individual elemental sites in such HEAs in enhancing the reactivity as well as the synergistic effects among the elements through density-functional-theory (DFT) calculations, which provides a new pathway for accelerating the discovery of highly efficient multi-elemental materials in energy catalysis [28]. Xu et al. further improved the efficiency of identifying highly catalytically active and stable catalysts through diversity-guided batch selection by employing an HEA multi-objective Bayesian optimization framework that simultaneously targets activity, cost-effectiveness, and entropic stability, which readily identifies a multitude of promising candidates for the oxygen reduction reaction in a hitherto uncharted HEA design space consisting of as many as 10 elements, thus striking a balance between all three objectives. three objectives [29]. Jiang et al. reported single-atom Pt-decorated nanoporous $Co_{0.85}Se$ (Pt/np-$Co_{0.85}Se$) as an efficient HER electrocatalyst. The developed Pt/np-$Co_{0.85}Se$ has an onset overpotential close to 0 and a Tafel slope as low as 35 mV $dec^{-1}$ for HER in neutral medium, which is superior to commercial Pt/C catalysts and other reported transition metal-based compounds. This work provides additional opportunities for local electronic restructuring of electrocatalysts to efficiently manipulate their catalytic properties through atomic-level engineering strategies [30].

In 1840, Joule was the first to describe the phenomenon of heat generation when current passes through conductive materials, known as Joule heating or Ohmic heating. He also proposed Joule's Law ($Q = I^2Rt$, where $Q$ is the heat generated, $I$ is the current, $R$ is the electrical resistance of the conductor, and $t$ is the time). Joule heating can be classified into two methods: indirect heating and direct heating. Indirect heating involves first heating a resistive metal coil and then transferring the generated heat to the precursor via radiation, convection, and conduction. Although convenient, this method results in lower power and heating rates. In contrast, direct Joule heating is widely favored because it directly heats the target through the current [31].

In order to enable the Joule heating method for the preparation and utilization of multicomponent alloy nanoparticle electrocatalysts, it is essential to select a stable and high-quality substrate. Carbon-based matrices are frequently used as material supports due to their excellent electrical conductivity, thermal conductivity, mechanical properties, and tunable specific surface area, which facilitate outstanding electrocatalytic performance [32–35]. The Carbon-based Thermal Shock (CTS) method, also known as High-Temperature Shock (HTS), operates based on the electrical Joule heating effect, enabling temperatures to rapidly reach thousands of Kelvins in just milliseconds. This results in exceptionally high heating and quenching rates, leading to significant structural transformations in materials. Moreover, this ultrafast synthesis and processing technique can produce novel, non-equilibrium structures that are impossible to achieve with traditional heating methods [36–39]. CTS technology has several distinct advantages: (1) It enables rapid heating and cooling; the high temperatures allow for instantaneous precursor decomposition, while ultrafast cooling prevents instantaneous metal aggregation. (2) The technology overcomes thermodynamic immiscibility in bimetallic systems, producing uniform, non-equilibrium bimetallic NPs. (3) By simply adjusting CTS parameters and the defect concentration of the carbon-based support, it is possible to precisely control elemental distribution, composition, microstructure, and particle size. (4) The instantaneous pulse heating method significantly reduces energy consumption while improving yield and productivity. As a result, CTS technology is highly sought after in the fields of energy storage and conversion [40,41].

In this work, we report a process for the rapid synthesis of alloy NPs on carbon substrates by introducing metal salts mixed in an ethanol solution and drop cast on commercial carbon paper, followed by rapid thermal synthesis. We also assess the HER performance of electrocatalysts with varying metal compositions under acidic conditions. By applying a pulsed voltage of 31 V during synthesis, the temperature of the commercial carbon paper is elevated from room temperature to approximately 1600 K within just about 2 s, resulting in the formation of uniformly distributed catalytic NPs on the carbon fibers. This CTS technique offers a straightforward and efficient approach for the rapid synthesis of alloy nanoparticle electrocatalysts on carbon substrates, demonstrating significant nanofabrication potential for a variety of other nanomaterials. Overall, our research provides an effective strategy for the efficient fabrication of metal nanoparticle-supported carbon-based electrocatalysts and their subsequent applications.

## 2. Experimental

In this study, the main premise was to design Pt-based alloy catalysts based on the following three aspects: (1) Pt is the state-of-the-art electrocatalyst that efficiently catalyzes the HER and is a good choice as the active site for the reaction [42]; (2) the atomic radii of Fe (1.34 Å), Ru (1.52 Å), Ni (1.49 Å), and Cu (1.45 Å) are smaller than that of Pt (1.77 Å), which creates compressive strain on the surface of the alloys, weakening the adsorption of H* on the surface Pt sites, thereby improving the catalytic performance for HER [43,44]; (3) lower cost by using non-precious metals [45].

### 2.1. Materials

$H_2PtCl_6$ (Merck, ACS reagent, ≥37.50 % Pt basis), $NiCl_2$ (IWG Austria), $RuCl_3$ (Roth, absolute 99.9 %, anhydrous), $FeCl_3$ (Roth, ≥98.5 %, anhydrous, extra pure) and $CuCl_2$ (Sigma-Aldrich, absolute 99.9 %). All chemicals were used as received primordially. Commercial carbon paper (Toray Carbon Paper, TGP-H-60) was cut to a uniform size (0.5 cm × 4 cm).

### 2.2. Synthesis of CP-X electrocatalysts

For the synthesis of the CP-PtM (M is Ni, Ru, Fe, Cu), The carbon paper required appropriate hydrophilic pretreatment to facilitate subsequent handling and reactivity. The specific procedures were as follows: the cut carbon paper was immersed in sulfuric acid solution (Roth, absolute 96 %) and maintained at 333K for 2 h. Afterwards, it was alternately washed with deionized water and ethanol (Australco Ethanol, absolute 99.9 %), then dried at ambient temperature. The mixture with a concentration of 0.05/n mol/L (n is the total number of elements) was dropped onto pretreated commercial carbon paper with a loading of 60 μL/$cm^2$ and dried at ambient temperature for 24 h. Fig. 1 (a) shows a schematic diagram of the carbothermal synthesis process of the metal NPs: the sufficiently dried carbon paper decorated with the metal salt solutions was quickly placed in a small vacuum plastic box and Joule-heated to high temperatures by applying a pulsed voltage

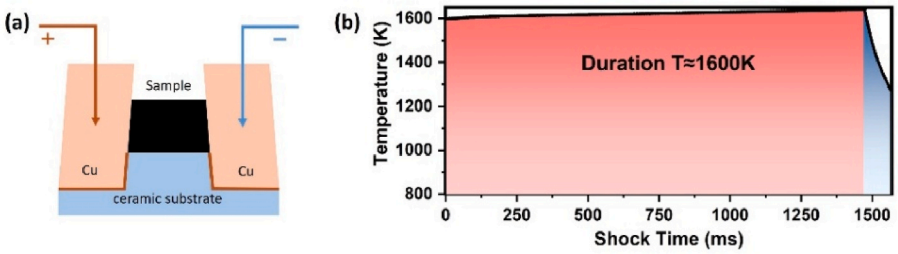


**Fig. 1.** (a) Schematic diagram of the Joule heating process and (b) Temporal evolution of the temperature during thermal shock.

(PeakTech 6226). The real-time temperature of the sample was monitored by a temperature sensor (Instrumart, OPTCTL3MH2CF3). The process of achieving instantaneous high temperature and rapid cooling resulted in the growth of fairly homogeneous metal NPs densely distributed on carbon fibers. The temperature and duration of the entire CTS process was precisely controlled by adjusting the parameters of the electrical pulse. In these experiments, a fixed voltage of 31 V was applied and the current was adjusted to rapidly increase the temperature of the samples to about 1600 K (Fig. 1 (b)). The samples were named CP-X (X is Pt, Ni, Ru, Fe, Cu) according to the metal elements introduced.

### 2.3. Characterizations

The surface morphology of the prepared catalysts was tested by scanning electron microscope (SEM, Zeiss, Leo 1525) using secondary electron detector. Energy-dispersive X-ray spectroscopy(EDS) using SEM (Tescan Magna) with 7 keV was used for compositional characterization of the samples. The X-ray diffraction (XRD, Bruker D2 Phaser) was occupied to characterize the crystal characteristics of the electrocatalysts. XPS (Nexsa, Thermofisher) equipped with an Al K Alpha source gun was used to study the surface elemental composition of the samples. The XPS was performed with an X-ray spot size of 400 μm, pass energy 50 eV, and energy step size 0.1 eV for high resolution scan. Reference calibration was performed using C 1s peak at 284.8 eV. A Varian 715-ES ICP optical emission spectrometer was used for element analysis. For sample dilution and preparation of standards, ultrapure water (MilliQ, Millipore) and ultrapure acids($HNO_3$ and HCl, Merck-Suprapure) were used. Standards were prepared in-house by dilution of certified, traceable, inductively coupled plasma (ICP)-grade single-element standards (Merck CertiPUR). Prior to ICP-MS analysis, the samples were diluted with 2 %v/v aqua regia to lower the background and interferences and reach the desired concentration range for measurement. Thermogravimetric analysis (TGA) was performed using a TGA/DSC 3 thermogravimetric analyzer (Mettler Toledo, OH, USA). Measurements were conducted in the temperature range of 25 °C–900 °C at a constant heating rate of 10 °C/min under a nitrogen atmosphere (flow rate: 50 mL/min). Upon reaching 900 °C, an isothermal hold was maintained for 10 min under an oxygen atmosphere (flow rate: 50 mL/min). Test samples, weighing between 0.8 mg and 1.3 mg, were placed in 70 μL $Al_2O_3$ crucibles for analysis. Data processing and result evaluation were carried out using STARe Evaluation Software (Mettler Toledo) and Origin (OriginLab Corporation). Local Raman spectra of CP before and after pretreatment, as well as CP-PtNiRu before and after electrochemical testing were acquired at a WITec alpha 300A using a green laser of 532 nm wavelength and a grating of 600 g/mm.

### 2.4. Electrochemical measurements

The Biologic SP-300 Electrochemical Potentiostat is a high-precision instrument widely used for electrocatalytic performance testing and analysis (e.g. cyclic voltammetry, linear scanning voltammetry and electrochemical impedance spectroscopy). All tests were conducted at room temperature.

The working electrode was an experimentally prepared electrode (0.25 $cm^2$), the counter electrode was a graphite electrode and the reference electrode was an Ag/AgCl electrode (sat. KCl). The performance of electrocatalytic HER was evaluated in nitrogen-saturated 0.5 M $H_2SO_4$ solution. Linear sweep voltammetry (LSV) was performed at a sweep rate of 10 mV/s. Tafel slopes were calculated from the LSV data. The electrochemical surface area (ECSA) was determined from the double layer capacitance ($C_{dl}$), which was derived from CVs recorded at different sweep rates (400-100 mV/s) in the non-Faraday potential range. Electrochemical impedance spectroscopy (EIS) measurements were performed in the frequency range of 10 mHz–100 kHz. Stability tests were carried out for a number of hours under constant potential conditions.

## 3. Results and discussion

Prior to the drop casting of metal salt solutions and Joule heating, we conducted a pretreatment of the carbon paper to enhance its wettability and susceptibility surface condition. Fig. 2 shows SEM images of the carbon paper before and after the acid pretreatment. Comparison of the morphology of the carbon paper substrate before (Fig. 2 (a)) and after (Fig. 2 (b)) acid treatment reveals that the surface morphology of the carbon paper remains uniform and smooth. Fig. 2 shows the preserved morphology of carbon fiber substrate structures without visible signs of significant changes in the microstructure after pretreatment.

Fig. 3 depicts SEM images of all samples after a series of drop-casting tests with metal salt solutions, drying and Joule heating treatment. It is evident that metal NPs with an approximate diameter of about 50 nm are uniformly dispersed across the carbon fibers. Furthermore, the comparison with the surface morphology of the pure carbon paper substrate shows that the morphological characteristics of the carbon fiber surface coated with the metal salt solutions changed significantly after the Joule heating, exhibiting a distinct porous structure, with a rougher fiber surface. This observed change is likely attributed to the thermal decomposition of the metal salt solutions during the rapid heating treatment, which generates gases and creates localized pressure on the carbon paper surface, resulting in the formation of pores. Additionally, as the temperature increases, the coalescence and migration of metal particles on the carbon paper surface contribute to localized structural collapse of the carbon fiber surface, further promoting pore formation.

To estimate the geometrical surface area of the NPs, we use ImageJ software to differentiate the alloy NPs from the carbon fiber area (Fig. S1). While Brunner Emmett-Teller (BET) surface area provides insight into the total porosity and nanostructure of the material, geometric surface area may offer a more realistic representation of the NPs on carbon fibers. Also, BET method could yield results that deviate from the actual value due to nature of its origin, which relies solely on physical adsorption. Unlike the reactivity of the NPs in electrochemical experiments, with only a portion of BET accessible surface may participate in the reaction due to mass transport and wetting limitations. While image processing from SEM images does not really represent the surface reactivity, it still gives impression on nanoparticle coverage

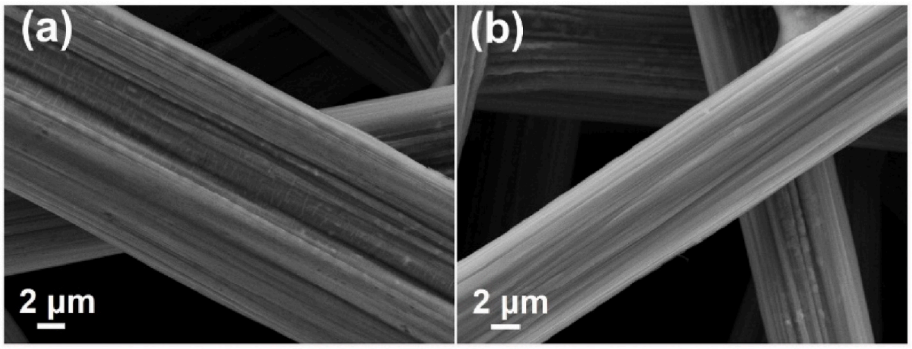


**Fig. 2.** SEM images of carbon felt-paper substrates (a) before pretreatment and (b) after pretreatment in acidic conditions prior to NP synthesis.

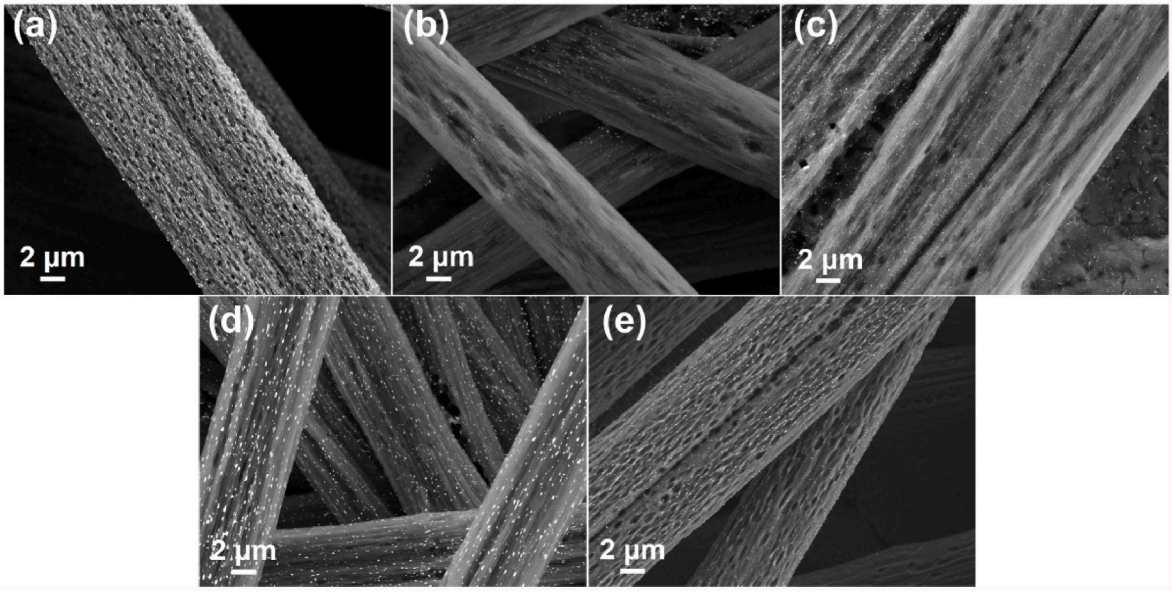


**Fig. 3.** SEM images of (a) CP-Pt; (b) CP-PtNi; (c) CP-PtNiRu; (d) CP-PtNiRuFe; (e) CP-PtNiRuFeCu showing successful fabrication of NPs by Joule heating method (cf. Fig. 1).

achieved by Joule heating, showing similar coverage of around 4 % across all NPs. It also enables us to observe that the size of NPs ranges from a few nms to aggerates of around 50 nm, with a broader NPs size distribution observed in both CP-PtNiRuFe and pure Pt NPs.

Furthermore, considering that the weight loss corresponds to organic binder by comparing it to pristine CP without any metal onto it, we calculated the metal loading by thermogravimetric analysis (TGA). TGA weight (%) plots are presented in Fig. S2. The calculations were based on the normalized weight loss and to the total mass of the material per surface area according to the following equation:

$$\text{Metal wt. \%} \times \text{total mass of material per cm}^2 = \text{Metal loading per cm}^2$$

Results of metal loading of all samples are provided in Table 1.

The resulting metal loading values are approximately 0.3 mg/cm$^2$ for all alloy combinations, exception for CP-PtNiRuFeCu, which shows a lower loading of 0.16 mg/cm$^2$. These findings support the assumption that Joule heating is an effective method for reducing Pt metal loading in alloy systems. These experimental values fall within the range typically used for HER studies [46,47] Moreover, with the addition of more metals to the alloy system, the relative Pt content is expected to decrease further, leading to even lower Pt loading. Therefore, this study highlights the potential of the Joule heating approach as a simple and scalable method for fabricating electrocatalytic electrodes aimed at reducing Pt usage.

**Table 1**
Metal loading of samples by TGA.

| Sample | wt.% metal/alloy (TGA) | Metal loading mg/cm$^2$ |
|---|---|---|
| CP-Pt | 7.30 | 0.30 |
| CP-PtNi | 6.34 | 0.27 |
| CP-PtNiRu | 6.76 | 0.29 |
| CP- PtNiRuFe | 8.06 | 0.33 |
| CP- PtNiRuFeCu | 4.76 | 0.16 |

To characterize the composition and crystal characteristics of the electrocatalysts, the samples were analyzed by X-ray diffraction (XRD). The XRD patterns are presented in Figure. The carbon paper substrate shows a dominant graphite peak at $2\theta = 30.6^\circ$ (Fig. 4(a)), which corresponded to the graphite 2H phase. This characteristic peak is also the most pronounced one in the XRD patterns of all other electrocatalyst samples, suggesting a dominant effect of the carbon fiber structure that significantly prevails the contribution of the NPs. At the same time, the peak intensities for the characteristic peak positions of the expected metallic phases are comparable to the noise level of the diffraction patterns. Thus, they are too small for a quantitative analysis. Comparing the theoretically calculated metal content and the XRD patterns, we attribute this to the small volume fraction of metal NPs in comparison with the carbon substrate. This result is also supported by the SEM images (Fig. 3) and explains why the peak intensities of the metal elements

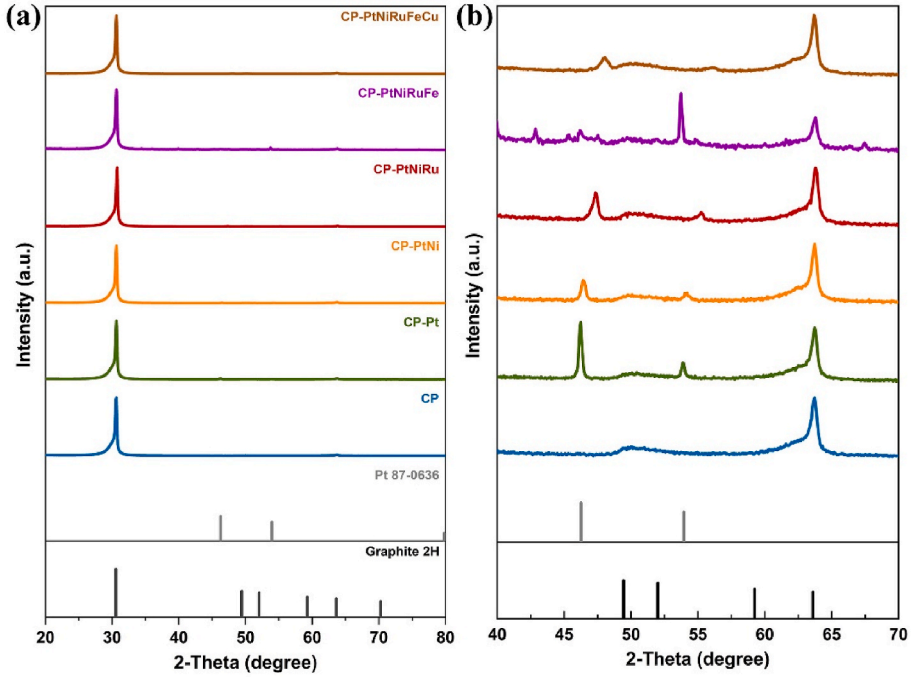


**Fig. 4.** (a) XRD patterns of plain carbon paper substrates after acid treatment (CP) and different alloy NPs synthesized on carbon paper substrates upon rapid thermal treatment; (b) Corresponding XRD patterns in the higher 2θ region (excluding the most intense graphite peak) revealing emerging peaks characteristic of the alloy NPs.

are much weaker than the peaks originating from the carbon substate. Only some weak characteristic peaks of Pt are observed at 46.3° and 53.9° because of the higher Pt loadings, indicating the face-centered cubic (FCC) structure of Pt in the samples.

To further investigate the spatial distribution of the introduced metal elements in the samples, we used EDS for comprehensive characterization of the top surface of the samples. The results are shown in Fig. 5. An electron energy of 7 keV was chosen for the tests, and the corresponding results outlining the composition of the samples by mapping of selected sample areas reveal the presence of all Pt-based mixed alloy NPs, as expected from the synthesis procedure. This result also confirms that we can successfully synthesize alloy NPs on the surface of the carbon paper used as a substrate by employing the Joule heating method at transient high temperatures and moderate time.

Individual NPs are labeled in the SEM images and analyzed for their elemental composition (Fig. 6).

High-magnification SEM images with EDS mapping show a heterogeneous distribution of alloy nanoparticle sizes (ranging from a few nm to about 50 nm) labeled in Fig. 5. The low acceleration voltage with 7 keV beam electrons reduces the interaction volume and increases the

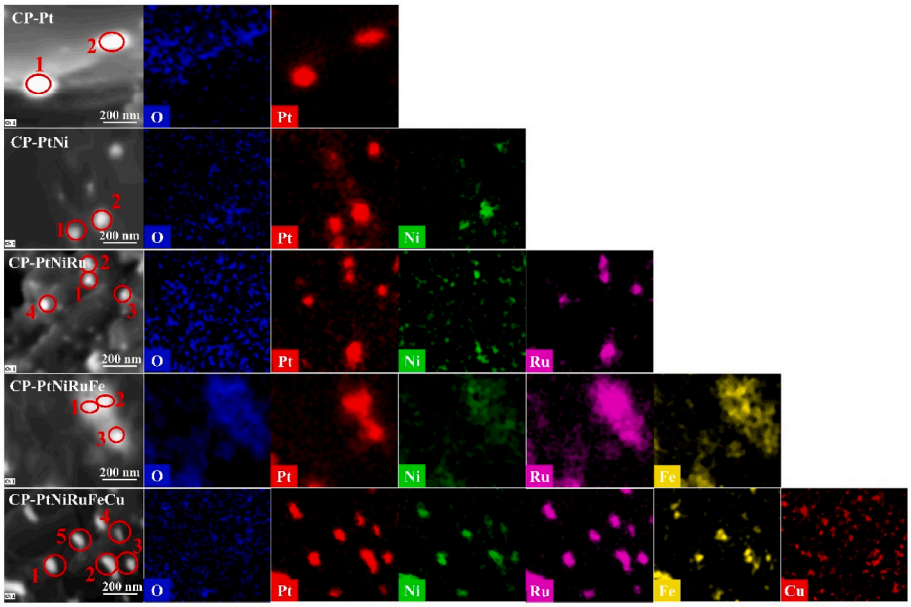


**Fig. 5.** SEM secondary electron images and elemental maps of integrated intensity from the EDS analysis for CP-Pt; CP-PtNi; CP-PtNiRu; CP-PtNiRuFe; CP-PtNiRuFeCu. The elemental maps are filtered and the contrast is adapted in order to display the spatial distribution of each element also for low integrated intensities and low signal to noise ratios.

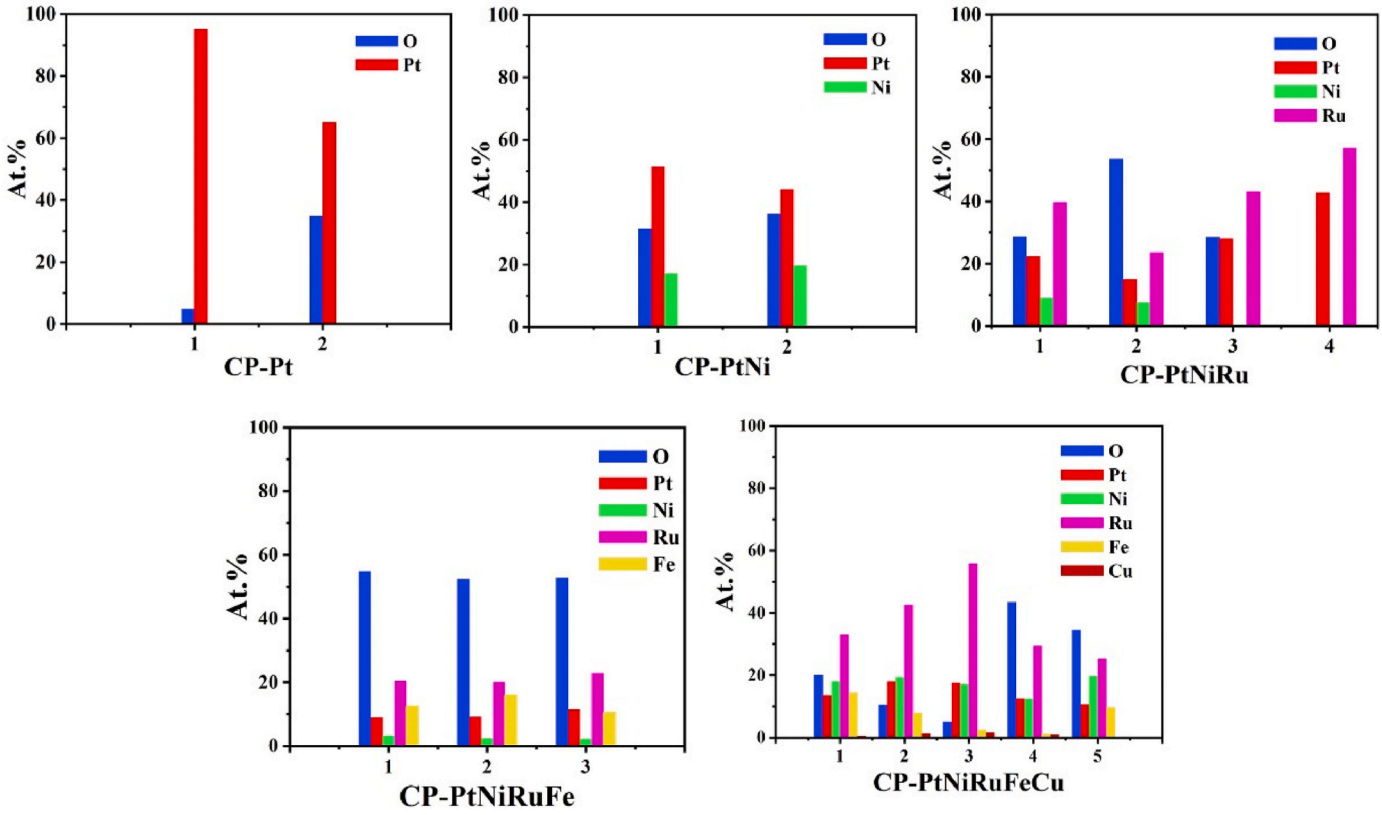


**Fig. 6.** Elemental composition in atomic % for all Pt-based alloy systems: CP-Pt; CP-PtNi; CP-PtNiRu; CP-PtNiRuFe; CP-PtNiRuFeCu. Separately analyzed NPs shown and labeled in Fig. 5 are numbered on the horizontal axis.

lateral resolution for EDS. Due to the fact, that the alloy NPs are located at the surface of the CP, the influence of the interaction volume is further reduced when analyzing the metal elements. Thus, the spatial resolution of the EDS analysis for the metal elements is greatly enhanced. A detailed analysis of the elemental composition of individual nanocrystals is given in Fig. 6. The spatial distribution of metal elements in the filtered elemental maps in Fig. 5 reveal that the metal elements are concentrated inside NPs, thus confirming the successful alloying process. For CP-PtNi and CP-PtNiRuFeCu a higher Ni content was achieved than in the cases of CP-PtNiRu and CP-PtNiRuFe. Also, high-resolution XPS spectra confirm the presence of Ni in the alloy NPs (Fig. S3). In contrast, Cu could not be alloyed to the NPs for the CP-PtNiRuFeCu system. The rather uniform distribution of Cu in Fig. 5 supports that finding. The elemental maps and an analysis of the elemental composition (Fig. 6) confirms the presence of surface bound oxygen on the samples. The oxygen spatial distribution differs depending on the alloying system. For CP-Pt, CP-PtNiRu and CP-PtNiRuFeCu the correlation between oxygen spatial distribution and nanoparticle areas is weak and the oxygen concentration varies between individual NPs. Thus, the NPs are metal NPs located at CP positions with a varying surface oxygen concentration. For CP-PtNi and CP-PtNiRuFe, the correlation between spatial oxygen distribution and nanoparticle areas is high and the oxygen concentrations of individual NPs are similar. For these alloying systems, the NPs are metal oxide NPs suggesting higher oxidation of transition metals.

The carbon support used in this work is commercial carbon paper with a thickness of more than 200 μm and fibers with a diameter of about 7 μm. However, for HR-TEM analysis, the sample thickness must be in the range of 10 nm. As a result, the overlap of thick fibers and NPs makes an HRTEM analysis impossible. Conventional sample preparing methods, such as mechanical milling and ion thinning, can easily damage the structure of the sample. Therefore, we used XPS and EDS to identify the elements and the compositions of the alloy NPs.

The core-level spectra of Pt 4f doublets (Pt $4f_{7/2}$ and Pt $4f_{5/2}$) of all compositionally alloyed NPs, obtained by Joule heating on carbon supports prior to electrochemical testing, are represented by XPS spectra in Fig. 7. The main photoelectron lines of Pt 4f spectra are deconvoluted into three parts to indicate the presence of Pt, $Pt^{2+}$, and $Pt^{4+}$. The two components of CP-Pt (Fig. 7 (a)) with lower binding energies (71.6 eV for Pt $4f_{7/2}$ and 74.9 eV for Pt $4f_{5/2}$) correspond to metallic Pt [48]. The doublets at 72.9 eV for Pt $4f_{7/2}$ and 76.4 eV for Pt $4f_{5/2}$ indicate the presence of $Pt^{2+}$ oxidation states, while the highest binding energies (75.2 eV for Pt $4f_{7/2}$and 78.4 eV for Pt $4f_{5/2}$) are associated with $Pt^{4+}$ [49]. Fig. 7(b)–(e) shows the Pt 4f peaks of CP-PtNi, CP-PtNiRu, CP-PtNiRuFe and CP-PtNiRuFeCu. Using CP-Pt as a reference, the binding energy of the Pt $4f_{7/2}$line for metallic Pt on CP-PtNiRu (Fig. 7(c), 71.6 eV) shows no significant shift, suggesting that the electronic state of Pt was not markedly affected by the presence of other metals in the alloy. However, since the catalytic activity of CP-PtNiRu was higher than that of CP-Pt, it can be inferred that the synergistic effect of Ni and Ru can effectively regulate the exposure of Pt active sites, thereby improving HER activity. Meanwhile, the Pt $4f_{7/2}$ peaks for CP-PtNiRuFe and CP-PtNiRuFeCu are shifted to higher binding energies, which could be due to the high electronegativity of Fe and Cu compared to Pt in these multicomponent alloys. This increased electronegativity could reduce electron transfer between the alloys, which is unfavorable for the redox reaction, causing the low catalytic activity of the Fe- and Fe–Cu-containing alloy NPs. Additionally, the data show that the $4f_{7/2}$ binding energy of $Pt^{2+}$ in the multimetal samples also shifted to higher binding energy, with CP-PtNiRu exhibiting the largest shift. This may be due to $Pt^{2+}$ being more readily reduced in this system, resulting in a shift of the Pt $4f_{7/2}$ to a higher binding energy. On the other hand, the binding energy of $Pt^{2+}$ on CP-Pt (72.9 eV) is lower than that of CP-PtNiRu (73.2 eV), indicating that the carboxyl groups on CP-PtNiRu may serve as

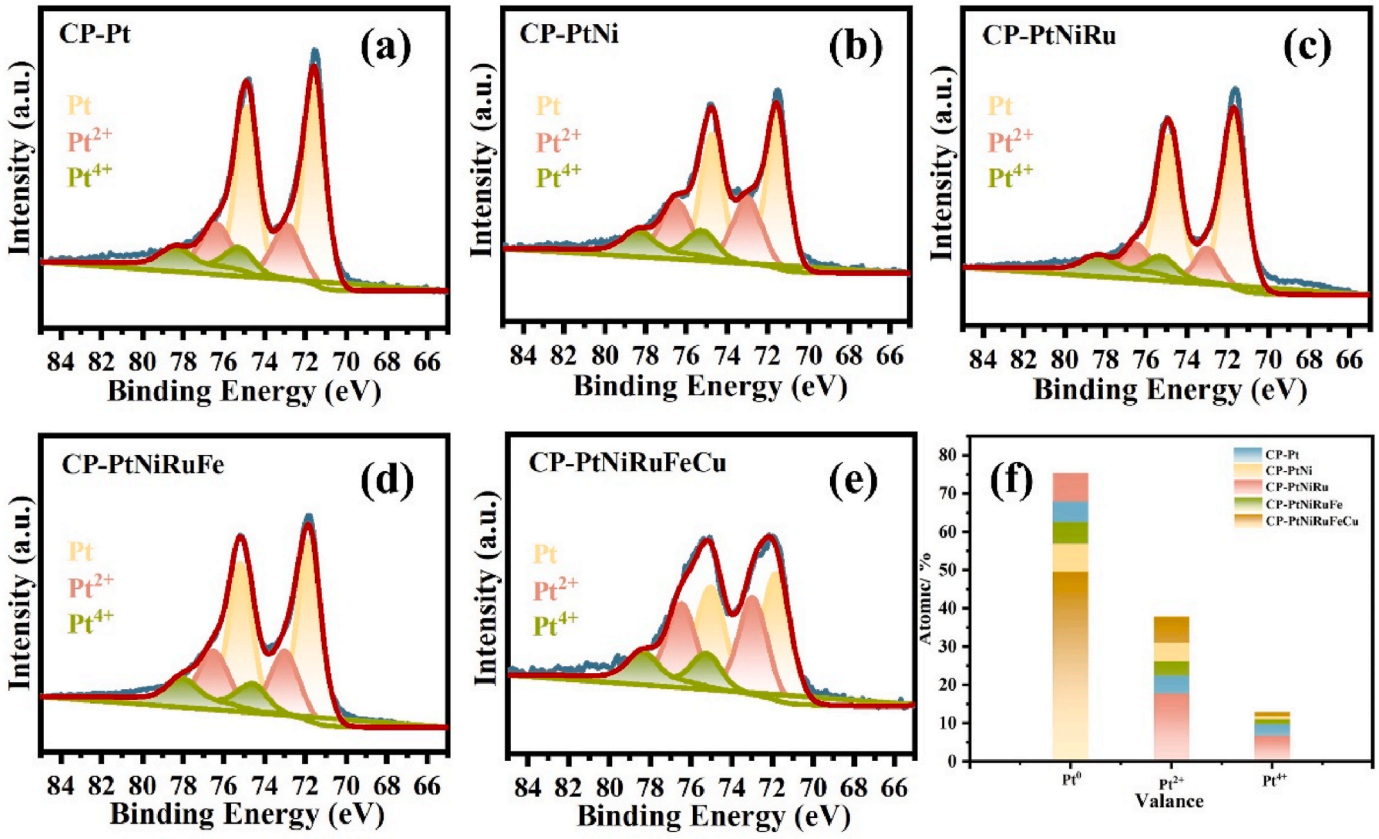


**Fig. 7.** High-resolution XPS spectra of Pt 4f of: (a) CP-Pt; (b) CP-PtNi; (c) CP-PtNiRu; (d) CP-PtNiRuFe; (e) CP-PtNiRuFeCu and (f) Atomic percentage distribution between three Pt valance states among all CP-Pt based catalysts, as calculated from respective and fitted XPS spectra depicted in (a)–(e).

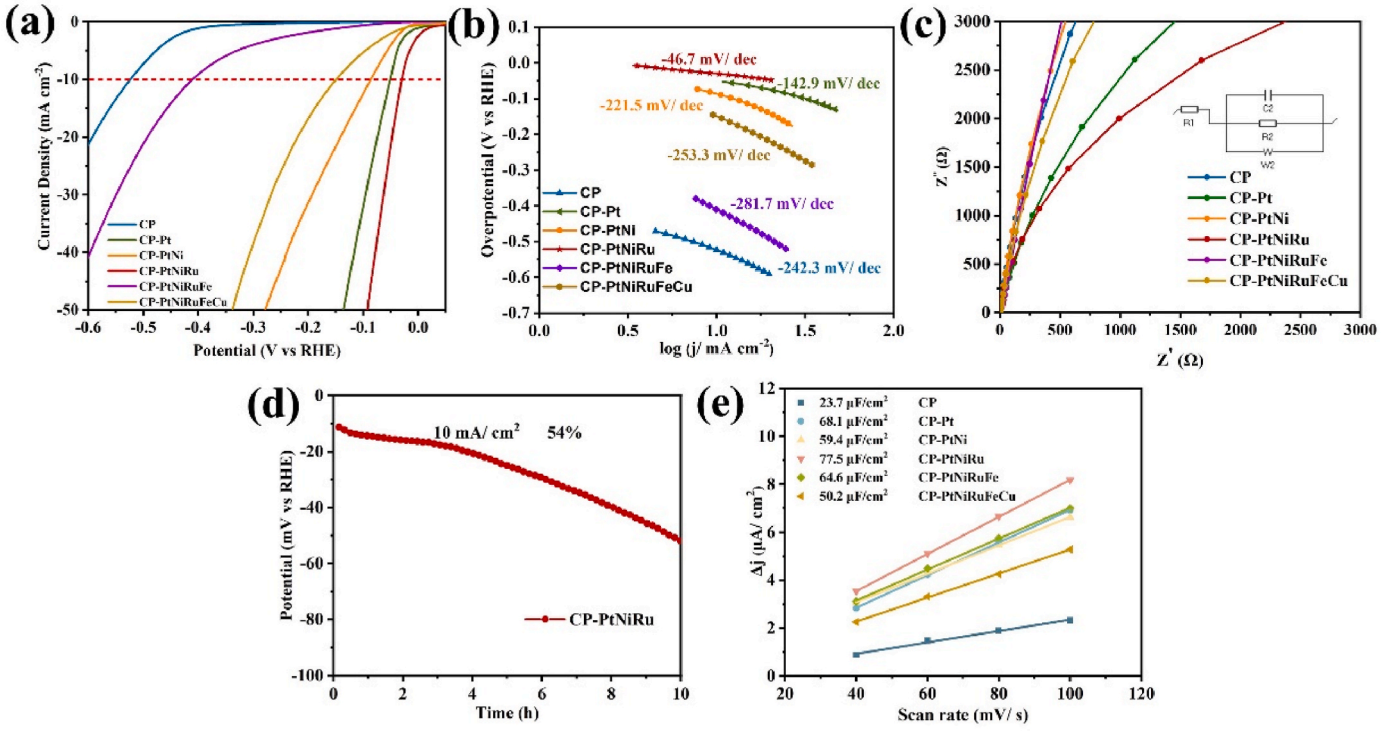


**Fig. 8.** (a) Linear Sweep voltammetry (LSV); (b) Tafel slopes; (c) Nyquist curves and (d) Electrochemical stability of CP-PtNiRu; (e) Electrochemical double-layer capacity ($C_{dl}$) of all samples.

anchoring sites for Pt, immobilizing it in the form of PtO (or PtOH). Fig. 7 (f) shows the high compositions of Pt followed by the compositions of its oxide states, which indicates that the as-synthesized NPs are predominantly Pt-metal. This also confirms that the chemical reduction process during preparation effectively transforms the $[PtCl_6]^{2-}$ species into metallic Pt. Nevertheless, small amount of $Pt^{2+}$ and $Pt^{4+}$ still presented in the alloy NPs, which could be due to the incomplete reduction of $Pt^{4+}$ in $H_2PtCl_6 \cdot 6H_2O$. The oxide status Pt were probably attributed to oxygen chemisorption on low-coordination sites of Pt NPs and residual $[PtCl_6]^{2-}$ species from the synthesis process [50].

Following the XPS analysis we compared the HER performance of all the samples.

First, the catalytic performance of the prepared samples using linear scanning voltammetry (LSV) was tested. Based on the dependence of the current density versus the potential, we further evaluated the ability of the catalyst to promote HER. The results are shown in Fig. 8 (a). As expected the pure carbon paper electrode exhibits a poor hydrogen evolution capability yielding a current density below 10 mA/cm$^2$ even under very negative applied potentials (−500 mV vs RHE). Contrary, the HER is more likely to occur when the carbon paper is decorated with metal NP electrocatalysts, indicating that all metal NPs used in this study possess HER activity.

Among the all samples, the PtNiRu alloy NPs electrocatalyst supported on carbon paper demonstrates the best HER performance with a lowest potential (~30.5 mV) that is even better than that of pure Pt NPs on carbon paper electrode (~50 mV) at 10 mA/cm$^2$.

To further understand the reaction kinetics, we recorded the linear part of the Tafel plot near a current density of 10 mA/cm$^2$ (Fig. 8 (b)). The Tafel slope for CP-PtNiRu (~46.7 mV/dec) is much lower than that of the other electrocatalysts, which suggests that this electrocatalyst has a strong ability to drive the HER process.

Next, we analyzed the electrode kinetics of all catalysts by electrochemical impedance spectroscopy (EIS) measurements (Fig. 8 (c)). The charge transfer resistance values (Rct) determined from semicircles recorded at low frequencies indicate that the CP-PtNiRu electrocatalysts have a higher charge transfer efficiency compared to pure carbon paper and CP-Pt electrocatalysts. The results of long-term voltage stability tests of the CP-PtNiRu conducted at a current density of 10 mA/cm$^2$ are shown in Fig. 8 (d).

The electrochemical active surface area (ECSA) of the catalysts was quantitatively evaluated by the electrochemical double-layer capacity method. Cyclic voltammetry (CV) scans were performed in the non-Faraday potential interval at scan rates of 40 mV/s, 60 mV/s, 80 mV/s and 100 mV/s. The results are shown in Fig. S4: (a)–(f) are CP; CP-Pt; CP-PtNi; CP-PtNiRu; CP-PtNiRuFe and CP- PtNiRuFeCu in order. The interfacial capacitance of the electrocatalysis (Fig. 8(e)) was obtained by calculating the current difference at various scan rates ($\Delta j=(j_a-j_c)/2$) and the linear fitting slope of different scan rates ($C_{dl}$). Considering the surface area of the CP that shows a lowest $C_{dl}$ (23.7μF/cm$^2$), calculated roughness factors of electrocatalysts yield an increase of about 2.1 as lowest for CP-PtNiRuCuFe to the highest of 3.3 of CP-PtNiRu that has the largest $C_{dl}$ (77.5 μF/cm$^2$). Thus, electrochemically accessible surface area of CP-PtNiRu stands out and corresponds to best HER activity among all electrocatalysts used in this study.

In Pt-based metal electrocatalyst systems, Pt serves as the main active center, exhibiting a low hydrogen adsorption free energy, which facilitates the HER process. Adding Ni not only reduces the amount of Pt required but also reduces the d-band center of Pt due to the interaction between Pt and Ni, facilitating the efficient adsorption of hydrogen and improving the overall HER activity [51]. The introduction of oxyphilic Ru accelerates water dissociation, and the carbon layer confinement further facilitates the water dissociation as well as subsequent *H adsorption, thus synergistically promoting the HER kinetics [52]. Additionally, the presence of Ni and Ru atoms modifies the d-band center of Pt, adjusting the hydrogen adsorption energy and optimizing the reaction pathway for HER [53]. In summary, the PtNiRu alloy NPs primarily enhance the HER activity through the synergistic effects of their constituent elements. The main reason why Fe-containing electrocatalyst systems fail to achieve ideal HER activity lies in the fact that Fe is prone to dissolution and corrosion under acidic conditions, resulting in the formation of Fe-ion byproducts and a loss of active sites. Additionally, compared to Pt and Ru, the synergistic effect between Fe and the carbon substrate is limited, leading to lower catalytic activity of the electrocatalyst [54].

Also, a comparison between the overpotential of CP-PtNiRu in this work and those of Pt-based electrodes from other recent studies (Table 2), which is included commercial Pt/C demonstrates its superior HER catalytic performance. Joule heating, as a fabrication method, allows for a simplified synthesis procedure of a variety of single or alloy NPs, making it a promising method for further optimization of the carbon support. It is well known that Ni is a bifunctional catalyst that exhibits excellent activity for both HER and OER [55–57]. Furthermore, recent studies highlight the synergetic effects of Ru single atoms adjunct to Ru nanoclusters, which tune the electronic structure and enhance HER performance [58].

As a challenge, platinum-based materials tend to leach from the support during the HER and detach over prolonged reaction times, which severely affects the electrochemical stability. Additionally, nickel tends to dissolve in the acidic conditions, which is another factor contributing to the poor stability of the electrocatalytic materials [66, 67]. Furthermore, the carbon support is highly susceptible to corrosion and dissolution after long term reactions in acidic electrolytes, leading to voltage instability [68,69]. To investigate the performance of CP-PtNiRu, the electrochemical stability tests were performed up to 60 h. The results shown in Fig. S5 suggest further degradation. XRD of CP-PtNiRu shows shift to higher 2θ suggesting Ru- rich structure (Fig. S6). To fully explore the potential of using this method and PtNiRu NPs as an efficient electrocatalyst for HER, a custom-made carbon support is needed. This would allow better optimization of adhesion and performance compared to the commercial carbon support.

In order to confirm our conjecture, we analyzed the surface of the CP-PtNiRu sample again after electrochemical testing (Fig. 9). It is obvious from Fig. 9 that after a long period of electrochemical testing, the carbon paper fibers fractured and the diameter of the loaded metal NPs increased significantly (from ~50 nm to ~200 nm). We assume that this might be due to the long-time electrochemical reaction resulting in some of the metal NPs interacting with the electrolyte on the surface of the carbon paper, subsequently generating secondary products leading to significant particle growth.

The NP coated carbon papers after electrochemical testing and purification were subjected to XPS measurements. The relative content of $Pt^0$ increases, while the $Pt^{2+}$ content decreases in CP-Pt, CP-PtNi and CP-PtNiRuFeCu samples after the HER reaction (Fig. 10). This effect could be attributed to easy dissolution of $Pt^{2+}$ and $Pt^{4+}$. However, the disappearance of the Pt 4f signal in CP-PtNiRuFe indicates poor stability of this alloy composition for HER. Moreover, considering the effect of Ni

**Table 2**
This work compared with other electrocatalysts.

| Catalysts | Overpotential (mV vs RHE) at 10 mA/cm$^2$ | Electrolytes | Source |
|---|---|---|---|
| CP-PtNiRu (this work) | 30.5 | 0.5 M $H_2SO_4$ | |
| $Cr_{0.6}Ru_{0.4}O_2$@MOF | 178 | 0.5 M $H_2SO_4$ | [59] |
| PtNi/NC-10 | 35 | 0.5 M $H_2SO_4$ | [60] |
| PtRu@$C_2N$ | 52 | 0.5 M $H_2SO_4$ | [61] |
| Surface-restructured PtRu alloy | 28 | 0.5 M $H_2SO_4$ | [62] |
| Pt/C | 30 | 0.5 M $H_2SO_4$ | [63–65] |

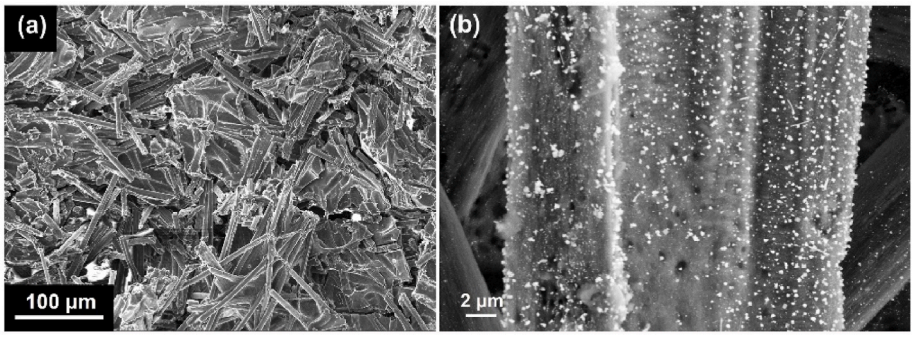


**Fig. 9.** SEM images of CP-PtNiRu after electrochemical stability testing.

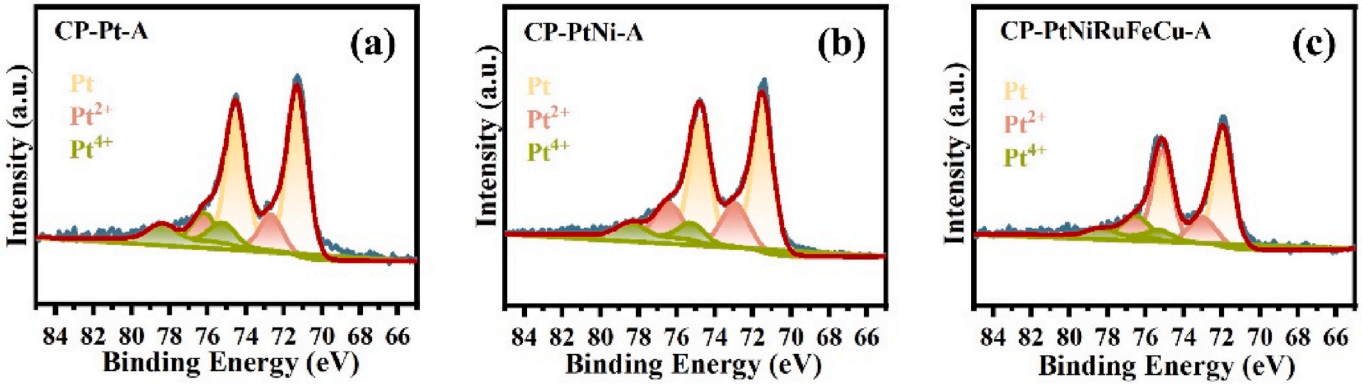


**Fig. 10.** High-resolution XPS spectra of Pt 4f of: (a) CP-Pt; (b) CP-PtNi; and (c) CP-PtNiRuFeCu after their testing as HER electrocatalysts.

dissolution in acidic solutions, we focus on the stability of the most active alloy, i.e., CP-PtNiRu. Assuming higher stability of the alloy particles, we aim to explore whether the dissolution of this alloy in acidic electrolyte (0.5 M $H_2SO_4$) leads to Ni leaching from the alloy NPs. In this context, we note that not only the dissolution of metal NPs but also the increased roughness and brittleness of carbon support particularly after prolonged electrochemical testing could influence the quality of XPS signal, resulting in the inability to detect the Pt 4f signal in the XPS spectra of CP-PtNiRu (Fig. S7).

To clarify the possible degradation mechanism of CP-PtNiRu, identified as the most active HER electrocatalyst in this study, we analyzed the metal content in the solution after prolonged electrochemical testing. ICP- MS results of the solution from CP-PtNiRu tested at a selected current density of 10 mA/cm$^2$ over a long time (ca. 60 h) show the expected dissolution of Ni. Interestingly, the Ni content is lower than initially assumed, and we also observe significant content of both Pt and Ru in the electrolyte after prolonged chronoamperometry testing of this catalyst (Table 3). Namely, the Pt:Ni:Ru ratio in the solution, as tested by the ICP-MS method, is 10:8:5, respectively, indicating that all the metal components in CP-PtNiRu are partially dissolved into the electrolyte during long electrochemical testing. We attribute this to the deterioration of the carbon support, not only dissolution of alloy NPs, during prolonged electrochemical testing. Therefore, despite the good results of one step NP fabrication on commercial carbon paper as the support and the good initial activity of CP-PtNiRu NPs (Fig. 8), we observe a significant decrease in activity over the testing period. This decrease can be ascribed not only to the dissolution of Ni but also to the influence on carbon fiber support. We assume that parts of the carbon fibers may have chipped away from the support, suggesting that the commercial carbon fiber is brittle. This is further supported by Raman analysis (Fig. 11).

**Table 3**
The ICP-MS result of concentration of metal elements in electrolyte of CP-PtNiRu after stability testing.

| Metal element | Concentration (mg/L) |
|---|---|
| Pt | 0.1 |
| Ni | 0.08 |
| Ru | 0.05 |

To further investigate the intrinsic reasons for the decrease in electrochemical stability of the electrocatalyst, Raman spectra using a green laser were acquired at single CP fiber positions after different steps of sample preparation: CP before (I) and after pretreatment (II), CP-PtNiRu after Joule heating (III) and after electrochemical testing (IV) (see Fig. 11). To separate overlapping Raman bands in the spectra (e.g., the characteristic carbon bands G at 1580 1/cm Raman shift and D' at 1620 1/cm Raman shift), the peaks were fitted with Pseudo-Voigt functions after background subtraction using the software fityk, as shown in Fig. 11 (a).

Fig. 11 (b) shows the ratios of the integrated Raman bands of single CP fibers with PtNiRu nanocrystals after the different preparation steps (I-IV) displayed in Fig. 11 (a). The $I_D/I_G$ ratio of each spectrum reveals defects in the CP fibers. C–H and O–H ratios are displayed relative to (I) the untreated CP, indicating chemical changes, possibly by contamination on the fibers.

It is worth noting that the signal is enhanced in the Raman shift region approximately between 1000 and 1700 1/cm after electrochemical testing, and additional bands appear on the background, indicating the presence of additional chemical compounds. Moreover, the integrated peak analysis shown in Fig. 11 (b) reveals a strong increase of C–H stretching vibrations after electrochemical testing (IV). In combination with the high $I_D/I_G$ integrated intensity ratio of carbon D and G bands in IV, these results demonstrate that the electrolyte used during testing affects the CP fibers. While the pretreatment of CP leads to no significant changes of the $I_D/I_G$ ratio, a first strong increase in the ratio occurs after Joule heating (III), followed by another strong increase after electrochemical testing (IV). The measured increase in carbon defects of CP

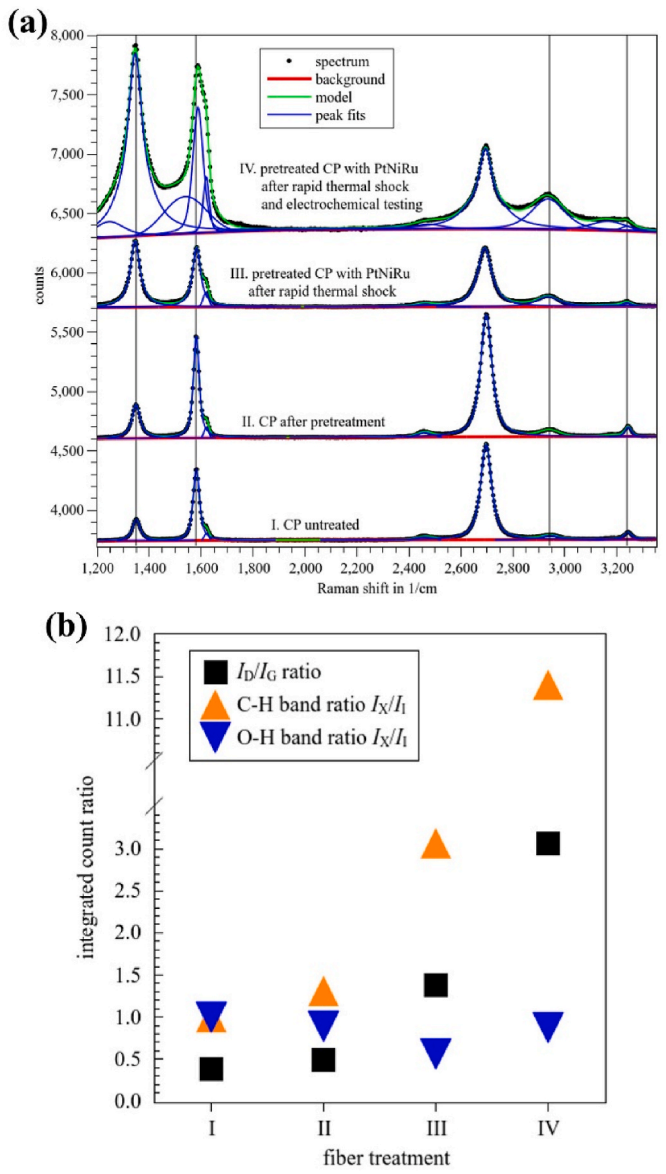


**Fig. 11.** Raman spectra (a) and Raman band ratios (b) of CP before (I) and after (II) pretreatment, CP-PtNiRu after Joule heating (III) and after electrochemical testing (IV).

agrees well with the SEM observations where pore formation is observed after step III and increased damaged (cut) CP fibers are observed after step IV, along with morphology changes of the PtNiRu NPs (cf. Figs. 3 and 8).

From the above results, it can be concluded that prolonged periods of electrochemical stability testing affect the carbon fiber structure of the substrate and the PtNiRu NPs significantly. Additionally, particle growth and the oxidation of metal NPs are accelerated, deteriorating the stability of the electrocatalyst.

While CP-PtNiRu demonstrated superior HER activity, the addition of Fe and Cu into Pt-based alloys aims at exploring potential synergistic effects, cost-effectiveness, and additional surface compositional alteration, which are also critical for practical catalyst design. In contrast to traditional alloys (e.g. binary, ternary or quaternary) having discrete binding energies, the present alloys gives broadened compositional space which could lead to continuous energy landscape. This is believed to be beneficial to match the optimal hydrogen binding strength according to classical Sabatier principle [70]. Despite not favorable HER activity for the alloys with Fe and Cu, understanding the structure–activity relationships in these multi-metallic systems contributes to the broader knowledge of catalyst development, even if the activity does not surpass that of CP-PtNiRu.

The stability of NPs is influenced by dissolution and oxide formation also in alloy NPs, the strategy to incorporate abundant elements such as Cu or Fe in form of alloy NPs aiming to increase their stability does not result in enhanced HER activity. In this context, this fabrication method, applied at moderate heating rates, offers ample opportunities to further tune catalytic activity and improve through the use of self-made carbon fiber supports. PtNiRu, in particular, could be a promising electrocatalyst of choice. However, further theoretical studies and deeper insights into degradation mechanisms are still needed to optimize catalyst performance.

## 4. Conclusion

In summary, we developed a synthesis process for carbon-supported Pt-based alloy nanoparticles with different compositions under high temperatures using a Joule heating method. Various methods were applied to study the structure, composition and electrocatalytic activity of the Pt-based alloy nanoparticles. The synthesis process employed on commercial carbon supports shows a broad size distribution of nanoparticles ranging from several nms up to 50 nm. The electrocatalytic activity of CP-Pt, CP-PtNi, CP-PtNiRu, CP-PtNiRuFe, and CP-PtNiRuFeCu identifies CP-PtNiRu as the most effective catalyst for hydrogen evolution reaction among all synthesized catalysts. The results indicate that the high activity of CP-PtNiRu stems primarily from the synergistic effect of introducing Ni and Ru into Pt and carbon support. Besides the alloy leaching, the decreasing stability over time of the CP-PtNiRu alloy is also impacted by the mechanical integrity that results in deterioration of carbon supports in acidic electrolyte. This method offers a novel strategy for further improvements by designing alloy nanoparticle-carbon matrix composite electrocatalysts and may be also applicable to other materials systems.

## CRediT authorship contribution statement

**Huanqing Zhang:** Writing – original draft, Visualization, Validation, Methodology, Investigation, Formal analysis, Data curation, Conceptualization. **Stefan Manuel Noisternig:** Writing – review & editing, Investigation, Formal analysis. **Qixiang Jiang:** Writing – review & editing, Investigation. **Martin Šala:** Investigation, Formal analysis. **Daniel Bautista – Anguis:** Investigation, Formal analysis. **Zequn Zhang:** Writing – review & editing, Software. **Stefan Wurster:** Writing – review & editing, Investigation. **Adam Elbataioui:** Writing – review & editing, Investigation. **Kaikai Song:** Writing – review & editing. **Christian Rentenberger:** Writing – review & editing, Validation, Formal analysis. **Lidija D. Rafailović:** Writing – review & editing, Visualization, Resources, Investigation, Conceptualization. **Jürgen Eckert:** Writing – review & editing, Resources.

## Declaration of interest statement

The authors declare that they have no known competing financial interests or personal relationships that could have appeared to influence the work reported in this paper.

## Acknowledgements

H.Z. acknowledges the financial support from the China Scholarship Council (CSC, Grant No. 202206220060). M. Š. acknowledges Slovenian Research and Innovation Agency (ARIS) research core funding no. P1-0034. We acknowledge support by S.M.N and the Faculty center for Nano Structure Research at the University Vienna. Furthermore, we thank Dr. Devinder Singh for useful discussions.

## Appendix A. Supplementary data

Supplementary data to this article can be found online at https://doi.org/10.1016/j.ijhydene.2025.150172.

## References


[1] Kovač A, Paranos M, Marciuš D. Hydrogen in energy transition: a review. Int J Hydrogen Energy 2021;46:10016–35. https://doi.org/10.1016/j.ijhydene.2020.11.256.

[2] Tiwari A. Hydrogen leading the green energy future. Adv Mater Lett 2022;13:2202. https://doi.org/10.5185/amlett.2022.021690. 1690.

[3] Dawood F, Anda M, Shafiullah GM. Hydrogen production for energy: an overview. Int J Hydrogen Energy 2020;45:3847–69. https://doi.org/10.1016/j.ijhydene.2019.12.059.

[4] Balat M. Potential importance of hydrogen as a future solution to environmental and transportation problems. Int J Hydrogen Energy 2008;33:4013–29. https://doi.org/10.1016/j.ijhydene.2008.05.047.

[5] Yue M, Lambert H, Pahon E, Roche R, Jemei S, Hissel D. Hydrogen energy systems: a critical review of technologies, applications, trends and challenges. Renew Sustain Energy Rev 2021;146:111180. https://doi.org/10.1016/j.rser.2021.111180.

[6] Li Y, Wei X, Chen L, Shi J. Electrocatalytic hydrogen production Trilogy. Angew Chem Int Ed 2021;60:19550–71. https://doi.org/10.1002/anie.202009854.

[7] Chen P, Ye J, Wang H, Ouyang L, Zhu M. Recent progress of transition metal carbides/nitrides for electrocatalytic water splitting. J Alloys Compd 2021;883:160833. https://doi.org/10.1016/j.jallcom.2021.160833.

[8] Fajrina N, Tahir M. A critical review in strategies to improve photocatalytic water splitting towards hydrogen production. Int J Hydrogen Energy 2019;44:540–77. https://doi.org/10.1016/j.ijhydene.2018.10.200.

[9] Zhao X, He D, Xia BY, Sun Y, You B. Ambient Electrosynthesis toward single-atom sites for electrocatalytic green hydrogen cycling. Adv Mater 2023;35. https://doi.org/10.1002/adma.202210703.

[10] Zhu J, Hu L, Zhao P, Lee LYS, Wong K-Y. Recent advances in electrocatalytic hydrogen evolution using nanoparticles. Chem Rev 2020;120:851–918. https://doi.org/10.1021/acs.chemrev.9b00248.

[11] Yu F-Y, Lang Z-L, Zhou Y-J, Feng K, Tan H-Q, Zhong J, et al. Revealing hydrogen evolution performance of single-atom platinum electrocatalyst with Polyoxometalate molecular models. ACS Energy Lett 2021;6:4055–62. https://doi.org/10.1021/acsenergylett.1c01911.

[12] Xu H, Shang H, Wang C, Du Y. Ultrafine Pt-based Nanowires for advanced catalysis. Adv Funct Mater 2020;30. https://doi.org/10.1002/adfm.202000793.

[13] Feng K, Xu J, Chen Y, Li S, Kang Z, Zhong J. Positively charged Pt-based Nanoreactor for efficient and stable hydrogen evolution. Adv Sci 2022;9. https://doi.org/10.1002/advs.202203199.

[14] Gao G, Zhu G, Chen X, Sun Z, Cabot A. Optimizing Pt-based alloy electrocatalysts for improved hydrogen evolution performance in alkaline electrolytes: a comprehensive review. ACS Nano 2023;17:20804–24. https://doi.org/10.1021/acsnano.3c05810.

[15] Ma W, Zhang X, Li W, Jiao M, Zhang L, Ma R, et al. Advanced Pt-based electrocatalysts for the hydrogen evolution reaction in alkaline medium. Nanoscale 2023;15:11759–76. https://doi.org/10.1039/D3NR01940C.

[16] Sun Z, Yang Y, Fang C, Yao Y, Qin F, Gu H, et al. Atomic-level Pt electrocatalyst synthesized via Iced photochemical method for hydrogen evolution reaction with high efficiency. Small 2022;18. https://doi.org/10.1002/smll.202203422.

[17] Liu J, Wang Z, Wu X, Zhang D, Zhang Y, Xiong J, et al. Pt doping and strong metal–support interaction as a strategy for NiMo-based electrocatalysts to boost the hydrogen evolution reaction in alkaline solution. J Mater Chem A Mater 2022;10:15395–401. https://doi.org/10.1039/D2TA03934F.

[18] Li C, Baek J-B. Recent advances in Noble metal (Pt, Ru, and Ir)-Based electrocatalysts for efficient hydrogen evolution reaction. ACS Omega 2020;5:31–40. https://doi.org/10.1021/acsomega.9b03550.

[19] Zhang C, Liang X, Xu R, Dai C, Wu B, Yu G, et al. H 2 in situ inducing strategy on Pt surface segregation over low Pt doped PtNi 5 Nanoalloy with superhigh alkaline HER activity. Adv Funct Mater 2021;31. https://doi.org/10.1002/adfm.202008298.

[20] Cui Z, Jiao W, Huang Z, Chen G, Zhang B, Han Y, et al. Design and synthesis of Noble metal-based alloy electrocatalysts and their application in hydrogen evolution reaction. Small 2023;19. https://doi.org/10.1002/smll.202301465.

[21] Ruqia B, Pt Choi S. Pt–Ni(OH) 2 electrodes for the hydrogen evolution reaction in alkaline electrolytes and their Nanoscaled electrocatalysts. ChemSusChem 2018;11:2643–53. https://doi.org/10.1002/cssc.201800781.

[22] Scofield ME, Zhou Y, Yue S, Wang L, Su D, Tong X, et al. Role of chemical composition in the enhanced catalytic activity of Pt-based alloyed Ultrathin Nanowires for the hydrogen oxidation reaction under alkaline conditions. ACS Catal 2016;6:3895–908. https://doi.org/10.1021/acscatal.6b00350.

[23] Jebaslinhepzybai BT, Prabu N, Sasidharan M. Facile galvanic replacement method for porous Pd@Pt nanoparticles as an efficient HER electrocatalyst. Int J Hydrogen Energy 2020;45:11127–37. https://doi.org/10.1016/j.ijhydene.2020.02.059.

[24] Li X, Huang Y, Chen Z, Hu S, Zhu J, Tsiakaras P, et al. Novel PtNi nanoflowers regulated by a third element (Rh, Ru, Pd) as efficient multifunctional electrocatalysts for ORR, MOR and HER. Chem Eng J 2023;454:140131. https://doi.org/10.1016/j.cej.2022.140131.

[25] Xiong L, Qiu Y, Peng X, Liu Z, Chu PK. Electronic structural engineering of transition metal-based electrocatalysts for the hydrogen evolution reaction. Nano Energy 2022;104:107882. https://doi.org/10.1016/j.nanoen.2022.107882.

[26] Oh A, Sa YJ, Hwang H, Baik H, Kim J, Kim B, et al. Rational design of Pt–Ni–Co ternary alloy nanoframe crystals as highly efficient catalysts toward the alkaline hydrogen evolution reaction. Nanoscale 2016;8:16379–86. https://doi.org/10.1039/C6NR04572C.

[27] Yang W, Cheng P, Li Z, Lin Y, Li M, Zi J, et al. Tuning the cobalt–platinum alloy regulating single-atom platinum for highly efficient hydrogen evolution reaction. Adv Funct Mater 2022;32. https://doi.org/10.1002/adfm.202205920.

[28] Pan Y, Shan X, Cai F, Gao H, Xu J, Zhou M. Accelerating the discovery of oxygen reduction electrocatalysts: high-throughput screening of element combinations in Pt-based high-entropy alloys. Angew Chem Int Ed 2024;63. https://doi.org/10.1002/anie.202407116.

[29] Xu W, Diesen E, He T, Reuter K, Margraf JT. Discovering high entropy alloy electrocatalysts in Vast composition spaces with Multiobjective optimization. J Am Chem Soc 2024;146:7698–707. https://doi.org/10.1021/jacs.3c14486.

[30] Jiang K, Liu B, Luo M, Ning S, Peng M, Zhao Y, et al. Single platinum atoms embedded in nanoporous cobalt selenide as electrocatalyst for accelerating hydrogen evolution reaction. Nat Commun 2019;10. https://doi.org/10.1038/s41467-019-09765-y.

[31] The scientific papers of James Prescott Joule. [n.d].

[32] Kuang P, Wang Y, Zhu B, Xia F, Tung C, Wu J, et al. Pt single atoms supported on N-doped Mesoporous Hollow carbon spheres with enhanced electrocatalytic H 2 -evolution activity. Adv Mater 2021;33. https://doi.org/10.1002/adma.202008599.

[33] Xiao Q, Yang J, Wang X, Deng Y, Han P, Yuan N, et al. Carbon-based flexible self-supporting cathode for lithium-sulfur batteries: progress and perspective. Carbon Energy 2021;3:271–302. https://doi.org/10.1002/cey2.96.

[34] Zhang W, Zhu S, Luque R, Han S, Hu L, Xu G. Recent development of carbon electrode materials and their bioanalytical and environmental applications. Chem Soc Rev 2016;45:715–52. https://doi.org/10.1039/C5CS00297D.

[35] Lai L, Li J, Deng Y, Yu Z, Wei L, Chen Y. Carbon and carbon/metal Hybrid structures enabled by ultrafast heating methods. Small Struct 2022;3. https://doi.org/10.1002/sstr.202200112.

[36] Wang H, Wang H, Zhang S, Zhang Y, Xia K, Yin Z, et al. Carbothermal shock enabled facile and fast growth of carbon nanotubes in a second. Nano Res 2022;15:2576–81. https://doi.org/10.1007/s12274-021-3762-8.

[37] Yao Y, Huang Z, Xie P, Lacey SD, Jacob RJ, Xie H, et al. Carbothermal shock synthesis of high-entropy-alloy nanoparticles. Science 1979;359:1489–94. https://doi.org/10.1126/science.aan5412. 2018.

[38] Ahn J, Park S, Oh D, Lim Y, Nam JS, Kim J, et al. Rapid Joule heating synthesis of oxide-socketed high-entropy alloy nanoparticles as CO 2 conversion catalysts. ACS Nano 2023;17:12188–99. https://doi.org/10.1021/acsnano.3c00443.

[39] Abdelhafiz A, Wang B, Harutyunyan AR, Li J. Carbothermal shock synthesis of high entropy oxide catalysts: dynamic structural and chemical Reconstruction boosting the catalytic activity and stability toward oxygen evolution reaction. Adv Energy Mater 2022;12. https://doi.org/10.1002/aenm.202200742.

[40] Zhang W, Wei X, Wu T, Wei F, Ma L, Lv Y, et al. Carbothermal shock enabled functional nanomaterials for energy-related applications. Nano Energy 2023;118:108994. https://doi.org/10.1016/j.nanoen.2023.108994.

[41] Shi W, Li Z, Gong Z, Liang Z, Liu H, Han Y-C, et al. Transient and general synthesis of high-density and ultrasmall nanoparticles on two-dimensional porous carbon via coordinated carbothermal shock. Nat Commun 2023;14:2294. https://doi.org/10.1038/s41467-023-38023-5.

[42] Greeley J, Jaramillo TF, Bonde J, Chorkendorff I, Nørskov JK. Computational high-throughput screening of electrocatalytic materials for hydrogen evolution. Nat Mater 2006;5:909–13. https://doi.org/10.1038/nmat1752.

[43] Wang D, Chen Z, Huang Y-C, Li W, Wang J, Lu Z, et al. Tailoring lattice strain in ultra-fine high-entropy alloys for active and stable methanol oxidation. Sci China Mater 2021;64:2454–66. https://doi.org/10.1007/s40843-020-1635-9.

[44] Escudero-Escribano M, Malacrida P, Hansen MH, Vej-Hansen UG, Velázquez-Palenzuela A, Tripkovic V, et al. Tuning the activity of Pt alloy electrocatalysts by means of the lanthanide contraction. Science 1979;352:73–6. https://doi.org/10.1126/science.aad8892. 2016.

[45] Kodama K, Nagai T, Kuwaki A, Jinnouchi R, Morimoto Y. Challenges in applying highly active Pt-based nanostructured catalysts for oxygen reduction reactions to fuel cell vehicles. Nat Nanotechnol 2021;16:140–7. https://doi.org/10.1038/s41565-020-00824-w.

[46] Yoo S, Kim Y, Yoon Y, Karuppannan M, Kwon OJ, Lim T. Encapsulation of Pt nanocatalyst with N-containing carbon layer for improving catalytic activity and stability in the hydrogen evolution reaction. Int J Hydrogen Energy 2021;46:21454–61. https://doi.org/10.1016/j.ijhydene.2021.03.225.

[47] Bal İB, Bulanık Durmuş GN, Devrim Y. Fabrication and performance evaluation of graphene-supported PtRu electrocatalyst for high-temperature electrochemical hydrogen purification. Int J Hydrogen Energy 2023;48:24369–84. https://doi.org/10.1016/j.ijhydene.2023.03.256.

[48] Peuckert M, Coenen FP, Bonzel HP. XPS study of the electrochemical surface oxidation of Platinum in N H2SO4 acid electrolyte. Electrochim Acta 1984;29:1305–14. https://doi.org/10.1016/0013-4686(84)87002-4.

[49] Bera P, Priolkar KR, Gayen A, Sarode PR, Hegde MS, Emura S, et al. Ionic dispersion of Pt over CeO 2 by the combustion method: structural investigation by XRD, TEM, XPS, and EXAFS. Chem Mater 2003;15:2049–60. https://doi.org/10.1021/cm0204775.

[50] Bugrova TA, Kharlamova TS, Svetlichnyi VA, Savel'eva AS, Salaev MA, Mamontov GV. Insights into formation of Pt species in Pt/CeO2 catalysts: effect of

treatment conditions and metal-support interaction. Catal Today 2021;375:36–47. https://doi.org/10.1016/j.cattod.2020.04.039.
[51] Ye W, Wu Z, Zhang S, Sun Y, Zhang X, Zhou W, et al. PtNi alloy nanoparticles grown in situ on nitrogen doped carbon for the efficient oxygen reduction reaction. Dalton Trans 2023;52:10817–27. https://doi.org/10.1039/D3DT01124K.
[52] Liu Z, Zhang H, Liu D, Feng Y, Jia D, Li C, et al. The critical role of Ru-like hydrogen adsorption of carbon dots in a carbon-confined Ru system for boosted HER activity. J Mater Chem A Mater 2024;12:8707–17. https://doi.org/10.1039/D3TA07016F.
[53] Hu T, Li P, Ye Y, Liu J, Cai Y, Liang C. Laser irradiation in liquid-generated PtNiRu@C nanoparticles for water hydrolysis. ACS Appl Nano Mater 2024;7:4865–73. https://doi.org/10.1021/acsanm.3c05607.
[54] Xu S, Zhao H, Li T, Liang J, Lu S, Chen G, et al. Iron-based phosphides as electrocatalysts for the hydrogen evolution reaction: recent advances and future prospects. J Mater Chem A Mater 2020;8:19729–45. https://doi.org/10.1039/D0TA05628F.
[55] Jiang M, Zhai H, Chen L, Mei L, Tan P, Yang K, et al. Unraveling the synergistic mechanism of Bi-functional nickel–iron phosphides catalysts for overall water splitting. Adv Funct Mater 2023;33. https://doi.org/10.1002/adfm.202302621.
[56] You S, Wu Y, Wang Y, He Z, Yin L, Zhang Y, et al. Pulse-electrodeposited Ni–Fe–Sn films supported on Ni foam as an excellent bifunctional electrocatalyst for overall water splitting. Int J Hydrogen Energy 2022;47:29315–26. https://doi.org/10.1016/j.ijhydene.2022.06.265.
[57] Van Phuc T, Jana J, Ravi N, Kang SG, Chung JS, Choi WM, et al. Highly active Ni/Co-metal organic framework bifunctional electrocatalyst for water splitting reaction. Int J Hydrogen Energy 2022;47:22787–95. https://doi.org/10.1016/j.ijhydene.2022.05.097.
[58] Ma J, Cho JH, Lee C, Kang MS, Choi S, Jang HW, et al. Unraveling the harmonious coexistence of ruthenium states on a self-standing electrode for enhanced hydrogen evolution reaction. Energy Environ Mater 2024. https://doi.org/10.1002/eem2.12766.
[59] Lin Y, Tian Z, Zhang L, Ma J, Jiang Z, Deibert BJ, et al. Chromium-ruthenium oxide solid solution electrocatalyst for highly efficient oxygen evolution reaction in acidic media. Nat Commun 2019;10. https://doi.org/10.1038/s41467-018-08144-3.
[60] Wang X, Che J, Wang T, Xu F, Duan D. Nitrogen-doped carbon nanosheet confined PtNi alloy for efficient acidic electrocatalytic hydrogen evolution reaction. Int J Hydrogen Energy 2024;91:735–43. https://doi.org/10.1016/j.ijhydene.2024.10.193.
[61] Li C, Zhang L, Zhang Y, Zhou Y, Sun J, Ouyang X, et al. PtRu alloy nanoparticles embedded on C2N nanosheets for efficient hydrogen evolution reaction in both acidic and alkaline solutions. Chem Eng J 2021;428. https://doi.org/10.1016/j.cej.2021.131085.
[62] Pang B, Liu X, Liu T, Chen T, Shen X, Zhang W, et al. Laser-assisted high-performance PtRu alloy for pH-universal hydrogen evolution. Energy Environ Sci 2022;15:102–8. https://doi.org/10.1039/d1ee02518j.
[63] Tavakkoli M, Holmberg N, Kronberg R, Jiang H, Sainio J, Kauppinen EI, et al. Electrochemical activation of single-walled carbon nanotubes with Pseudo-atomic-scale platinum for the hydrogen evolution reaction. ACS Catal 2017;7:3121–30. https://doi.org/10.1021/acscatal.7b00199.
[64] McCrory CCL, Jung S, Ferrer IM, Chatman SM, Peters JC, Jaramillo TF. Benchmarking hydrogen evolving reaction and oxygen evolving reaction electrocatalysts for solar water splitting devices. J Am Chem Soc 2015;137:4347–57. https://doi.org/10.1021/ja510442p.
[65] Liu X, Hao S, Zheng G, Su Z, Wang Y, Wang Q, et al. Ultrasmall Pt2Sr alloy nanoparticles as efficient bifunctional electrocatalysts for oxygen reduction and hydrogen evolution in acidic media. J Energy Chem 2021;64:315–22. https://doi.org/10.1016/j.jechem.2021.04.065.
[66] Ferreira EB, Tahmasebi S, Jerkiewicz G. On the catalytic activity and corrosion behavior of polycrystalline nickel in alkaline media in the presence of neutral and reactive gases. Electrocatalysis 2021;12:146–64. https://doi.org/10.1007/s12678-020-00637-4.
[67] Angeles-Olvera Z, Crespo-Yapur A, Rodríguez O, Cholula-Díaz J, Martínez L, Videa M. Nickel-based electrocatalysts for water electrolysis. Energies (Basel) 2022;15:1609. https://doi.org/10.3390/en15051609.
[68] Kim Y, Jun SE, Lee G, Nam S, Jang HW, Park SH, et al. Recent advances in water-splitting electrocatalysts based on electrodeposition. Materials 2023;16:3044. https://doi.org/10.3390/ma16083044.
[69] Talukder N, Wang Y, Nunna BB, Lee ES. An in-depth exploration of the electrochemical oxygen reduction reaction (ORR) phenomenon on carbon-based catalysts in alkaline and acidic mediums. Catalysts 2022;12:791. https://doi.org/10.3390/catal12070791.
[70] Xu W, Diesen E, He T, Reuter K, Margraf JT. Discovering high entropy alloy electrocatalysts in vast composition spaces with multiobjective optimization. J Am Chem Soc 2024;146:7698–707. https://doi.org/10.1021/jacs.3c14486.